

An Accretion-Modulated Internal Shock Model for Long GRBs

R. MORADI,¹ C. W. WANG,^{1,2} E. S. YORGANCIOLU,^{1,2} AND S. N. ZHANG^{1,2}¹*State Key Laboratory of Particle Astrophysics, Institute of High Energy Physics, Chinese Academy of Sciences, Beijing 100049, China.*²*University of Chinese Academy of Sciences, Chinese Academy of Sciences, Beijing 100049, China*

ABSTRACT

We introduce the *Accretion-Modulated Internal Shock model* (AMIS) as a possible framework for explaining the observational properties of long gamma-ray burst (GRB) prompt emission. In this scenario, the envelope of the prompt light curve follows the time-dependent mass-supply history to the central engine, associated with stellar collapse and, where applicable, fallback accretion, whose early-time onset can be approximated by $\dot{M} \propto t^{0-1/2}$ and which subsequently may decay as $\dot{M} \propto t^{-5/3}$, producing a photon count rate with a single fast-rise–exponential–decay (FRED)–like profile. In general, the prompt-emission envelope is regulated by a time-dependent mass supply to the central engine, while internal shocks produce the rapid variability. Since we only aim to introduce this framework here, we focus on the simplest single-FRED shape of the prompt emission profiles, while more complex cases involving multiple episodes and interacting shocks will be explored in forthcoming studies. The model indicates correlations between spectral evolution, FRED-pulse narrowing at high energies, and the mass-supply–controlled envelope. Stochastic Lorentz-factor variations of ejected mass- or rate-driven shells, superimposed on the Accretion-Modulated envelope, explain the coexistence of smooth global trends and irregular short-timescale features, such as the widths of individual pulses in long GRB light curves, offering diagnostic tools for probing the inner engine activity.

1. INTRODUCTION

The light curves of gamma-ray bursts (GRBs) in their prompt emission episode usually display rapid, multi-peaked variability, traditionally interpreted within the framework of internal shocks (IS) among the succession of ultra-relativistic shells emanated from the inner engine (Rees & Meszaros 1994; Sari & Piran 1996, 1997; Kobayashi et al. 1997; Daigne & Mochkovitch 1998; Zhang 2018; Bošnjak et al. 2022; Bošnjak et al. 2009; Bošnjak & Daigne 2014). Thanks to the high resolution of missions such as the Burst and Transient Source Experiment (*BATSE*; 20–2000 keV) (Fishman et al. 1985), Fermi’s Gamma-ray Burst Monitor (GBM; 8 keV–40 MeV) (Meegan et al. 2009), Konus-Wind (20–20000 keV) (Aptekar et al. 1995), the Hard X-ray Modulation Telescope (HXMT; 1–3000 keV) (Zhang et al. 2018, 2020), and the Gravitational wave high-energy Electromagnetic Counterpart All-sky Monitor (GECAM; 6–6000 keV; Li et al. 2022; An et al. 2022; Zhang et al. 2023; Wang et al. 2024), prompt-phase light curves now provide valuable information not only about the radiation mechanisms but also about the temporal behavior of mass and energy injection

associated with the central engine (Kobayashi et al. 1997; Daigne & Mochkovitch 2003; Hascoët et al. 2012; Maxham & Zhang 2009). Empirically, several studies have reported systematic correlations among temporal observables such as pulse waiting times, full width at half-maximum (FWHM), and peak fluxes, in addition to stochastic variability. Such correlations suggest that the shell-production process is modulated by a varying driver, possibly linked to the structure or evolution of the inner engine, rather than purely random fluctuations (MacFadyen et al. 2001; Nakar & Piran 2002; Bhat et al. 2012; Guidorzi et al. 2015; Maccary et al. 2026).

Internal shock models successfully capture the observed nonthermal spectra and variable pulse structure (e.g., Kobayashi et al. 1997; Nakar & Piran 2002; Bošnjak & Daigne 2014). However, the systematic temporal trends reported in many bursts are still not well accounted for within IS models (see e.g., Moradi et al. 2024). At the same time, core-collapse simulations show that fallback of bound stellar debris onto the compact remnant produces a time-dependent mass-supply rate whose late-time evolution follows $\dot{M}(t) \propto t^{-5/3}$ and may exhibit an early-time onset consistent with $\dot{M}(t) \propto t^{0-1/2}$ (Chevalier 1989; MacFadyen et al. 2001; Kumar et al. 2008; Jacquemin-Ide et al. 2024). This behavior sustains long-duration energy injection, and when coupled to a relativistic outflow whose luminosity follows the time-dependent mass supply to the central

engine, produces a fast-rise–slow-decay (FRED)–like envelope. Therefore, it can imprint broad temporal trends on the prompt light curve. Stochastic variations in the Lorentz factor of the ejected shells riding on top of this mass-supply–regulated envelope can then produce the observed fine-scale multi-peaked structure. In this framework, namely the Accretion-Modulated internal shock (AMIS) model, pulse properties such as FWHM, waiting times, and amplitude evolution emerge as the combined result of time-dependent mass-supply histories (fallback-dominated where applicable) and internal shock physics.

The fallback-accretion–driven framework has been utilized to account for the early afterglow flares in some GRBs (e.g., Wu et al. 2013; Geng et al. 2013). Signatures consistent with fallback-regulated mass-supply decay have also been reported in the afterglow of ultra-long GRBs such as GRB 250702B (Zhang et al. 2025). However, direct application to the prompt phase remains limited, and a model connecting mass-supply–controlled (fallback-dominated where applicable) broad envelopes with variable internal shocks has not yet been fully developed. In this paper, we introduce the *Accretion-Modulated Internal Shock model* as a general framework for long GRB prompt emission, in which a phenomenological, time-dependent mass-supply history to the central engine—arising from stellar collapse and including fallback as a physically motivated limiting case—is mapped onto shell ejection and internal-shock dissipation. We discuss its predictions for temporal and spectral observables, and highlight how it can account for both global light-curve trends and fine-scale stochastic variability.

The paper is organized as follows. In Section 2, we review fallback accretion in collapsars and its role in regulating the time-dependent mass supply that shapes the broad temporal envelope of GRB prompt emission. In Section 3 we introduce the mathematical foundation of the AMIS model by describing shell-collision dynamics. We further present in Section 4 the framework that maps the time-dependent mass-supply history onto shell properties within two representative modulation scenarios. We then examine the spectral evolution of pulses and derive analytic estimates for band-limited pulse widths in Section 5. Section 6 summarizes our findings and discusses implications for central-engine physics and progenitor structure, together with caveats and possible avenues for future improvement.

2. FALBACK-REGULATED MASS SUPPLY AND JET LUMINOSITY IN COLLAPSARS

Long GRBs are widely interpreted as the collapse of massive, rapidly rotating stars that form either a black hole or a neutron star, capable of launching relativistic jets. In the collapsar framework, two evolutionary channels are pro-

posed: Type I and Type II collapsars (e.g., MacFadyen & Woosley 1999; Popham et al. 1999; Fryer et al. 1999; Wang & Mészáros 2007). The mass supply to the central engine is intrinsically time-dependent and may involve both prompt collapse-driven mass accretion and delayed fallback of bound stellar material, depending on the progenitor structure and explosion outcome (e.g., MacFadyen et al. 2001; Narayan et al. 2001).

In Type I collapsars, the black hole promptly forms with a hyper-accreting disk of typical accretion rates $\dot{M} \sim 10^{-2} - 1 M_{\odot} \text{ s}^{-1}$, depending on the progenitor structure, angular momentum, and disk viscosity (MacFadyen & Woosley 1999; Popham et al. 1999). Such high rates are capable of efficiently powering relativistic jets via neutrino annihilation or magnetohydrodynamic (MHD) processes. Assuming a radiative efficiency $\epsilon_{\text{rad}} \sim 0.01 - 0.2$, the isotropic-equivalent prompt luminosities can therefore reach $L_{\text{prompt}} \sim 10^{53} \text{ erg s}^{-1}$, consistent with the majority of observed long GRBs. Immediate black hole formation is thus typically associated with bright prompt emission, while any precursor activity is expected to be weak or absent, with additional variability arising primarily from jet propagation effects.

Type II collapsars occur when the initial explosion is weak or fails, leaving a proto-neutron star while a significant fraction of the stellar envelope remains gravitationally bound. Subsequent fallback of marginally bound material then occurs on timescales $t_{\text{fb}} \sim 1 - 10^3 \text{ s}$ (Chevalier 1989; Fryer et al. 1999; Zhang et al. 2008). If sufficient mass is accreted, the proto-neutron star collapses into a black hole, potentially enabling the delayed launching or re-energization of a relativistic jet. Typical fallback rates are smaller, $\dot{M} \sim 10^{-3} - 10^{-2} M_{\odot} \text{ s}^{-1}$, for which neutrino cooling and annihilation are inefficient (Popham et al. 1999), leading to lower radiative efficiency. The resulting prompt luminosities are therefore expected to lie in

$$L_{\text{prompt}} \sim 10^{47} - 10^{49} \text{ erg s}^{-1},$$

unless magnetic energy extraction (e.g., Blandford–Znajek) dominates (Komissarov & Barkov 2009). Type II collapsars thus provide a natural explanation for underluminous GRBs, precursor activity, and gradually rising prompt-emission light curves.

At this stage, the time-dependent mass-supply profile is adopted as a phenomenological description of the central-engine evolution, without attempting a detailed classification of individual GRBs. A quantitative classification based on detailed light-curve morphology, energetics, and spectral evolution will be developed in future work.

In Type II collapsars, the mass supply to the central engine is dominated by the fallback of marginally bound stellar material, which naturally exhibits a well-defined early-

time onset followed by a late-time decay that approaches a power-law scaling $\propto t^{-5/3}$ in self-similar fallback solutions (MacFadyen et al. 2001; Wu et al. 2013). To capture this behavior in a flexible yet physically motivated manner, we adopt a smooth, fallback-motivated *time-dependent mass-supply* profile to parameterize the engine feeding history in Type II systems.

Specifically, we employ the following functional form for the mass-supply rate:

$$\dot{M}(t) = \dot{M}_p \left[\frac{1}{2} \left(\frac{t - t_0}{t_p - t_0} \right)^{-s/2} + \frac{1}{2} \left(\frac{t - t_0}{t_p - t_0} \right)^{5s/3} \right]^{-1/s}, \quad (1)$$

where \dot{M}_p is the peak mass-supply rate, t_0 marks the onset of engine activity, t_p denotes the time of peak mass delivery, and s controls the smoothness of the transition between the rising (onset) and decaying phases. This prescription is intended to represent a *generic, smoothly evolving mass-supply history* with a well-defined onset, peak, and decay, rather than a unique or universal fallback solution.

Classical fallback provides one physically motivated realization of such a mass-supply history, particularly relevant for delayed-collapse (Type II) collapsars, but the AMIS framework itself does not require fallback to dominate the mass budget in all realizations. Instead, the adopted form serves as a convenient and physically grounded parameterization of time-modulated engine feeding. Such configurations may be especially relevant for low-luminosity GRBs, including GRB 980425, where mildly relativistic ejecta and internal-shock dissipation have been invoked to explain the prompt emission within a collapsar context (e.g., Daigne & Mochkovitch 2007).

For Type I collapsars, the accretion is driven by prompt infall through a hyperaccreting disk capable of powering a relativistic jet (MacFadyen & Woosley 1999; Narayan et al. 2001). The detailed temporal evolution of the accretion rate in such prompt-collapse scenarios remains uncertain and depends sensitively on the progenitor structure and angular-momentum profile. It is nevertheless expected to be more strongly peaked and shorter-lived than the extended fallback accretion characteristic of Type II collapsars, with a rapid decline of the *engine power* once the dense stellar core has been exhausted (MacFadyen et al. 2001; Gottlieb 2025), rather than a $t^{-5/3}$ fallback-dominated phase (Chevalier 1989).

In this work, we nevertheless employ the same functional form (Equation 1) for Type I collapsars as a *parametric modeling convenience*. This choice allows us to explore, in a unified manner, how a time-modulated engine power imprints global trends on the prompt emission, while explicitly recognizing that the late-time $t^{-5/3}$ behavior is not physically motivated for prompt-collapse events. Indeed, a more rapidly

declining engine power is more effective to producing the sharply decaying “exponential” tail commonly observed in classical FRED light curves (Norris et al. 1996, 2005). In practice, for Type I collapsars the model parameters can be chosen to encode a more intense and short-lived accretion episode than in Type II systems. Future multidimensional simulations of collapsar accretion and jet launching will be required to replace this prescription with a more physically realistic description of $\dot{M}(t)$ in prompt-collapse systems.

The instantaneous jet (engine) power is parameterized as

$$\dot{E}_{\text{jet}}(t) = \eta \dot{M}(t) c^2, \quad (2)$$

where η , which varies in the range $\sim 10^{-3} - 0.1$, accounts for the efficiency of converting rest-mass energy into jet power, encompassing neutrino, MHD, or spin-extraction processes (Popham et al. 1999; Komissarov & Barkov 2009). For the parameter ranges primarily explored in this work, the implied peak accretion rates, $\dot{M}_p \sim 10^{-2} - 10^{-1} M_{\odot} \text{ s}^{-1}$, are consistent with hyperaccreting inner flows commonly inferred for Type I collapsar GRB engines, depending on the disk structure and accretion geometry. Lower peak accretion rates, $\dot{M}_p \sim 10^{-3} - 10^{-2} M_{\odot} \text{ s}^{-1}$, may also be realized in Type II collapsar scenarios, particularly when combined with higher radiative or internal-shock efficiencies.

Accordingly, the time-dependent mass supply to the central engine is assumed, when accretion conditions permit, to power a relativistic outflow whose injected energy is partially converted into non-thermal radiation via internal dissipation processes such as shocks or magnetic reconnection. The observable prompt gamma-ray luminosity is then parameterized as

$$L_{\gamma}(t) = \epsilon_{\text{rad}} \dot{E}_{\text{jet}}(t) = \epsilon_{\text{rad}} \eta \dot{M}(t) c^2, \quad (3)$$

where ϵ_{rad} denotes the radiative efficiency, i.e. the fraction of jet power converted into gamma-ray emission (e.g., Mészáros 2006; Kumar & Zhang 2015).

For typical GRB parameters, a substantial fraction of this prompt emission is expected to arise from synchrotron radiation of relativistic electrons accelerated within internal dissipation regions of the jet. The characteristic photon energy can be estimated as

$$E_{\text{syn}} \propto \Gamma B' \gamma_e^2, \quad (4)$$

where Γ is the bulk Lorentz factor of the jet, B' is the comoving magnetic field, and γ_e is the Lorentz factor of the radiating electrons. For typical values ($\Gamma \gtrsim 300$, $B' \sim 10^4 - 10^5$ G, $\gamma_e \sim 10^2 - 10^4$), synchrotron emission can naturally produce photons in the 100–1000 keV range, consistent with observed prompt GRB spectra (e.g., Kumar & Zhang 2015; Mészáros 2006).

Throughout this work, the term “Accretion-Modulated” is used in a phenomenological sense to denote a time-dependent mass-supply history regulating the engine power.

Classical fallback provides one physically motivated realization of such modulation, but the AMIS framework does not require fallback to dominate the accretion flow.

3. ACCRETION-MODULATED INTERNAL SHOCKS (AMIS)

3.1. Kobayashi-Piran-Sari (KPS) Collision Dynamics for Two/Multiple Shells

Internal shocks (ISs) were first modeled as collisions of discrete shells (Kobayashi et al. 1997). In its multi-shell scenario, the succession of shells emanate from the inner engine. Therefore, the long-term light curve reflects the central-engine activity, while local fluctuations arise from stochastic variations in shell masses and Lorentz factors. If the engine drives a secular trend in shell ejection—such as one set by a time-dependent fallback accretion rate—the same trend is expected to appear in the IS light curve because observed pulse times map approximately one-to-one onto engine ejection times.

A nonuniform relativistic wind may therefore be represented as a sequence of shells, with two-shell collisions as the elementary dissipation process. A faster shell (r) catches a slower one (s), merging into a new shell (m); energy-momentum conservation gives the Lorentz factor of the merged shell (Kobayashi et al. 1997). Superposed pulses from successive collisions reproduce the observed temporal variability. For two colliding cold shells,

$$\gamma_m = \left[\frac{m_r \gamma_r + m_s \gamma_s}{m_r / \gamma_r + m_s / \gamma_s} \right]^{1/2}, \quad (5)$$

$$E_{\text{int}} = m_r c^2 (\gamma_r - \gamma_m) + m_s c^2 (\gamma_s - \gamma_m), \quad (6)$$

where γ_m is the post-collision bulk Lorentz factor and E_{int} is the internal (dissipated) energy. The corresponding radiative efficiency is

$$\epsilon = 1 - (m_r + m_s) \gamma_m / (m_r \gamma_r + m_s \gamma_s). \quad (7)$$

The Lorentz factors of the forward and reverse shocks are given by (Kobayashi et al. 1997):

$$\gamma_{\text{fs}} \simeq \gamma_m \sqrt{\frac{1 + 2\gamma_m / \gamma_s}{2 + \gamma_m / \gamma_s}}, \quad \gamma_{\text{rs}} \simeq \gamma_m \sqrt{\frac{1 + 2\gamma_m / \gamma_r}{2 + \gamma_m / \gamma_r}}, \quad (8)$$

with corresponding velocities $\beta_{\text{fs}} = \sqrt{1 - \gamma_{\text{fs}}^{-2}}$ and $\beta_{\text{rs}} = \sqrt{1 - \gamma_{\text{rs}}^{-2}}$.

The merged shell width is calculated as (Kobayashi et al. 1997):

$$l_m = l_s \frac{\beta_{\text{fs}} - \beta_m}{\beta_{\text{fs}} - \beta_s} + l_r \frac{\beta_m - \beta_{\text{rs}}}{\beta_r - \beta_{\text{rs}}}, \quad (9)$$

where l_s and l_r are the widths of the slow and rapid shells, and β_m , β_s , β_r are the velocities of the merged, slow, and rapid shells respectively.

The reverse-shock crossing (emission) time and the curvature (angular) timescale are estimate as

$$\delta t_e = \frac{l_r}{c(\beta_r - \beta_{\text{rs}})}, \quad \tau_{\text{ang}} = \frac{R}{2\gamma_m^2 c}, \quad (10)$$

where l_r is the shell width in the lab frame, β_{rs} is the velocity of the reverse shock, and R is the collision radius.

The analytic pulse shape proposed by Kobayashi et al. (1997) is adopted as

$$L_{\text{KPS}}(t) = h \begin{cases} 1 - \frac{1}{(1 + t/\tau_{\text{ang}})^2}, & 0 < t < \delta t_e / (2\gamma_m^2), \\ \frac{1}{(1 + t/\tau_{\text{ang}} - \Delta)^2} - \frac{1}{(1 + t/\tau_{\text{ang}})^2}, & t > \delta t_e / (2\gamma_m^2), \end{cases} \quad (11)$$

where $\Delta \equiv c\delta t_e / R$ and $h = (2\gamma_m^2 / \delta t_e) E_{\text{int}}$ ensures $\int L_{\text{KPS}}(t) dt = E_{\text{int}}$.

3.2. Multiple-Shell Collisions

In this scenario, we assume that the central engine releases a sequence of shells in a single, short-lived activity envelope episode without long quiescent intervals. At the lab-frame time $\tilde{t} = 0$, when the last shell is emitted, the inner edges of the shells are located at

$$R_i(0) = -\tilde{t}_i \beta_i c, \quad \beta_i = \sqrt{1 - \gamma_i^{-2}}, \quad (12)$$

where \tilde{t}_i is the shifted ejection time such that $\tilde{t}_N = 0$ for the last shell. The separation between shells i and $i + 1$ is

$$L_i = R_i - R_{i+1} - l_{i+1}. \quad (13)$$

Following Kobayashi et al. (1997), the collision time between two adjacent shells (inner faster, outer slower) is

$$\delta t_{i,i+1} = \frac{L_i}{c(\beta_{i+1} - \beta_i)}, \quad (14)$$

which is positive only when $\beta_{i+1} > \beta_i$.

For $N > 2$ shells, collisions are handled recursively. At each step, the minimum $\delta t_{i,i+1}$ is selected, the system time is advanced by that amount, and the colliding pair merges using the conservation relations. The complete merging procedure is: 1) Calculate merged Lorentz factor γ_m using equation 5; 2) Calculate internal energy E_{int} using equation 6; 3) Calculate reverse and forward shock Lorentz factors γ_{fs} , γ_{rs} using equations 8; 4) Calculate merged shell width l_m using equation 9; 5) Update shell properties: γ_m , $m_m = m_r + m_s$, and l_m .

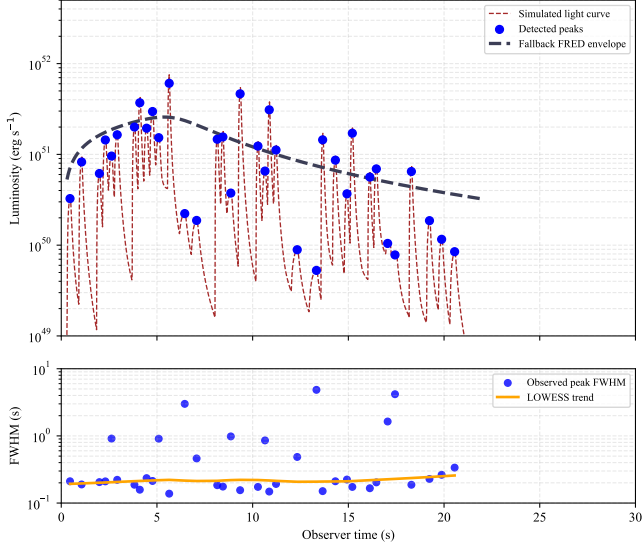


Figure 1. Simulated GRB prompt-emission light curves from an Accretion-Modulated internal-shock (AMIS) model. **Mass-driven scenario.** The fast-rise, slow-decay shape of the envelope is imposed by a time-dependent, accretion-regulated mass-supply history of the central engine, associated with stellar collapse and accretion-driven mass delivery, which modulates the ejected shell masses ($m_0 = 3 \times 10^{28}$ g, $t_0 = 0.1$ s, $t_p = 6$ s, $s = 5$, and lab-frame widths $l_i \in [10^9, 2 \times 10^9]$ cm) at roughly constant ejection intervals. Stochastic variations in shell Lorentz factors ($\Gamma_i \in [400, 800]$) generate internal shocks, producing the fine-scale, multi-peaked structure typical of GRB light curves. The simulation yields a total dissipated energy $E_{\text{diss}} \simeq 1.036 \times 10^{52}$ erg, a total initial kinetic energy $E_{\text{kin}} \simeq 5.542 \times 10^{53}$ erg, and a time-averaged radiative efficiency $\epsilon \simeq 0.019$. Pulse FWHMs are measured from the observed peaks of the smoothed light curve, ensuring that closely spaced or merged collisions are treated as single pulses. The resulting FWHMs remain approximately constant, reflecting the nearly uniform hydrodynamic and angular timescales associated with fixed ejection intervals. A locally weighted smoothing (LOWESS) of the individual pulse widths highlights only minor fluctuations around this overall flat trend.

The observed arrival time of the corresponding pulse is

$$t_{\text{obs}} = (1 + z) \left[t_{\text{col}} - \frac{R_c(t_{\text{col}})}{c} \right], \quad (15)$$

where $R_c(t_{\text{col}})$ is the collision radius, z is the cosmological redshift of the source, and the earliest t_{obs} is set to zero.

The approximate one-to-one mapping between engine ejection times and observed pulse times can be verified by equating shell trajectories. Consider two shells ejected by the central engine: a slower shell (s) at $t = 0$ with velocity $\beta_s c$, and a faster shell (r) at $t = \Delta t_{\text{ej}}$ with velocity $\beta_r c > \beta_s c$. Their positions in the lab frame are

$$R_s(t) = \beta_s c t, \quad R_r(t) = \beta_r c (t - \Delta t_{\text{ej}}), \quad t > \Delta t_{\text{ej}}. \quad (16)$$

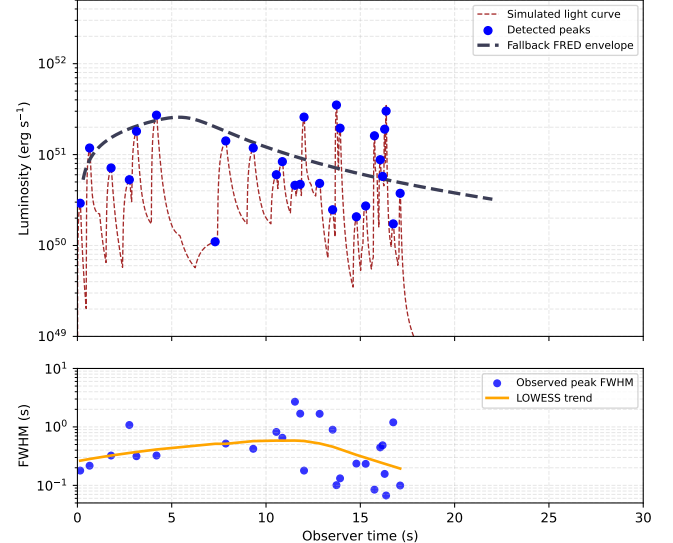


Figure 2. Simulated GRB prompt-emission light curves from an Accretion-Modulated internal-shock (AMIS) model. **Rate-driven scenario.** Shell ejection intervals follow the time-dependent, accretion-regulated mass-supply history, while the shell masses remain nearly constant ($m_i \sim 3 \times 10^{28}$ g). Random fluctuations in the Lorentz factors cause shells to collide at irregular intervals, generating internal shocks that imprint variability on the light curve. The simulation yields a total dissipated energy $E_{\text{diss}} \simeq 1.526 \times 10^{52}$ erg, a total kinetic energy $E_{\text{kin}} \simeq 1.062 \times 10^{54}$ erg, and a time-averaged radiative efficiency $\epsilon \simeq 0.014$. Pulse FWHMs evolve with the mass-supply rate: pulses are narrower and brighter during phases of lower mass supply and broader and dimmer during phases of higher mass supply. The trend is derived using locally weighted smoothing over individual pulse widths to highlight the overall temporal evolution.

The collision occurs when the shells meet, $R_s(t_{\text{col}}) = R_r(t_{\text{col}})$, which gives the lab-frame collision time

$$t_{\text{col}} = \frac{\beta_r}{\beta_r - \beta_s} \Delta t_{\text{ej}}. \quad (17)$$

The collision radius is then

$$R_c = R_s(t_{\text{col}}) = \frac{\beta_r \beta_s}{\beta_r - \beta_s} c \Delta t_{\text{ej}}. \quad (18)$$

Accounting for the light-travel delay to the observer, the arrival time of photons is

$$t_{\text{obs}} = t_{\text{col}} - \frac{R_c}{c} = \frac{\beta_r (1 - \beta_s)}{\beta_r - \beta_s} \Delta t_{\text{ej}}. \quad (19)$$

For ultra-relativistic shells ($\beta_i \simeq 1 - 1/(2\gamma_i^2)$), this reduces to

$$t_{\text{obs}} \simeq \frac{\gamma_r^2}{\gamma_r^2 - \gamma_s^2} \Delta t_{\text{ej}}. \quad (20)$$

Hence, for $\gamma_r \gg \gamma_s$, we have $t_{\text{obs}} \approx \Delta t_{\text{ej}}$, demonstrating that the observed pulse times approximately trace the engine ejection times. This justifies the one-to-one mapping

between central-engine activity and observed internal-shock pulses.

4. MASS-SUPPLY-MODULATED TEMPORAL TREND

To link the KPS internal-shock scenario with a time-dependent mass supply to the central engine, as an illustrative realization, we adopt a fallback-motivated mass-delivery history. To account for both the initial onset of mass delivery and the post-peak decay, we consider a function similar to Equation 1, which captures the full temporal evolution of the mass-supply history:

$$\dot{M}_{\text{ms}}(t) \propto \begin{cases} t^{\beta_{\text{onset}}}, & t < t_{\text{peak}}, \\ t^{-5/3}, & t \geq t_{\text{peak}}, \end{cases} \quad (21)$$

with $\beta_{\text{onset}} \simeq 0\text{--}0.5$ (MacFadyen et al. 2001). Here $\dot{M}_{\text{ms}}(t)$ denotes the time-dependent *mass-supply rate to the engine/disk*.

The time-dependent mass-supply rate to the central engine modulates the properties of the emitted shells, which can be implemented through a time-dependent normalization factor ($h = (2\gamma_m^2/\delta t_e)E_{\text{int}}$) of the KPS luminosity in Equation (11):

$$h_j(t_{\text{obs}}) = A \left(\frac{t_{\text{obs}}}{t_{\text{ref}}} \right)^{\beta_{\text{eff}}(t_{\text{obs}})} \propto \dot{M}_{\text{ms}}(t), \quad (22)$$

where

$$\beta_{\text{eff}}(t_{\text{obs}}) = \begin{cases} \beta_{\text{onset}}, & t_{\text{obs}} < t_{\text{peak}}, \\ -5/3, & t_{\text{obs}} \geq t_{\text{peak}}, \end{cases} \quad (23)$$

$t_{\text{ref}} = 1\text{ s}$, and A is chosen to conserve energy. The proportionality reflects the assumption that, to leading order, the dissipated energy per collision traces the engine mass-supply history, with the mapping between engine time and observer time treated approximately.

For the envelope in this AMIS framework, we specifically refer to the broad, smooth luminosity evolution of GRBs whose prompt emission profiles exhibit a single fast-rise-exponential-decay (FRED) segment. These events provide a clean testbed for isolating mass-supply-modulated physics. In multi-pulse events, each sub-envelope may correspond to a distinct episode of enhanced mass delivery or modulation of the engine feeding history, giving rise to compound FRED-like structures similar to those observed in several BATSE and GBM bursts (Hakkila & Preece 2014). Since this work represents the first introduction of the AMIS framework, we focus on the simplest single-envelope configurations; more complex cases involving multiple mass-supply modulation episodes will be investigated in forthcoming studies.

In fact, single-pulse, FRED-like GRBs constitute a significant subset of the long-GRB population. Early BATSE analyses already highlighted the prevalence of such smooth FRED profiles among bright bursts (Norris et al. 1996), and a more recent systematic study of 2710 Fermi GRBs based on objective automated criteria found that almost half of the long bursts can be classified as predominantly single-peaked (Hintze 2022).

It is worth noting that in many Type II collapsar scenarios the late-time mass-supply history to the central engine can decay as a power law, typically with index $\sim -5/3$ after its peak time, as expected for the self-similar fallback of marginally bound ejecta in physically motivated cases. Moreover, as shown by Ryde & Svensson (2000, 2002), in a substantial fraction of GRBs the late-time portion of the photon flux curves is better described by a power-law decay, $N(t) \propto t^{-n}$, with n between about 1 and 2. This behavior arises when both the hardness–intensity correlation (HIC) and the hardness–fluence correlation (HFC) hold, producing a natural transition from exponential-like early decay to power-law tails in the photon flux. Within the AMIS framework, this suggests that even if individual pulses begin with an approximately exponential decay, the cumulative emission from successive internal shocks, driven by an engine whose injection is regulated by a declining mass-supply history, can imprint a late-time power-law decay in $N(t)$, and consequently in the observed flux, consistent with the empirical findings of Ryde & Svensson (2000, 2002); Peng et al. (2012).

4.1. Mass-Driven vs. Rate-Driven Scenarios

We consider two distinct ways in which a time-dependent mass-supply history to the central engine can modulate the prompt emission of gamma-ray bursts. These two channels are representatives to capture the whole picture. In a physical setting, complex and complicated forms of mass-supply modulation are expected.

In the *mass-driven scenario*, shells are emitted at roughly constant intervals, $\Delta t_{\text{ej}} \simeq \Delta t_0$, while the mass of each shell follows the time-dependent mass-supply history:

$$m_i \simeq \dot{M}_{\text{ms}}(t_i) \Delta t_0 \propto t_i^{\beta_{\text{eff}}(t_i)}. \quad (24)$$

Consequently, before the peak of the mass-supply rate, pulse amplitudes grow with time ($\beta_{\text{eff}} > 0$), while after the peak they decay with $\beta_{\text{eff}} \simeq -5/3$. With stochastic Lorentz-factor fluctuations among the ejected shells, the dissipated energy approximately tracks the underlying shell-mass trend ($E_{\text{int}} \propto m_i$), while the hydrodynamic and angular timescales that determine the pulse FWHM follow only the mild fluctuations of the Lorentz factors and therefore maintain an overall near-constant trend across collisions. This leads to mass-driven pulses that exhibit energy growth during the rising phase and decay after the peak of the mass-supply history,

while their FWHM remain approximately constant. Such behavior is in line with observational studies indicating that pulse widths in long GRBs show little or no systematic temporal evolution (Ramirez-Ruiz & Fenimore 2000).

Our numerical simulation of $N_{\text{shells}} = 70$ shells with initial masses modulated by a smooth FRED-like mass-supply envelope ($m_0 = 3 \times 10^{28}$ g, $t_0 = 0.1$ s, $t_p = 6$ s, $s = 5$, and lab-frame widths $l_i \in [10^9, 2 \times 10^9]$ cm) and stochastic Lorentz factors in the range $\Gamma_i \in [400, 800]$ produces a prompt-emission light curve consistent with AMIS expectations; see Figure 1. The simulation yields a total dissipated energy $E_{\text{diss}} \simeq 1.036 \times 10^{52}$ erg and a total initial kinetic energy $E_{\text{kin}} \simeq 5.542 \times 10^{53}$ erg, corresponding to a time-averaged radiative efficiency $\epsilon \simeq 0.019$.

In our simulations the shells are not sorted by Lorentz factor, and no *a priori* ordering is imposed. Each shell is assigned an ejection time according to the prescribed engine sequence, and its Lorentz factor is drawn independently from a uniform (linear) distribution within the stated range. Internal shocks then arise self-consistently when a faster shell emitted at a later time catches up with a slower shell emitted earlier. Different random realizations change the detailed pulse morphology (e.g., exact peak times and amplitudes), as expected in stochastic internal-shock models, but do not alter the qualitative AMIS trends discussed here.

The above values are physically consistent with a hyperaccreting collapsar engine, representative of a Type I realization, in which the time-dependent mass supply to the central engine is regulated primarily by collapse-driven mass delivery, with possible contributions from delayed feeding. Assuming a typical accretion-to-outflow efficiency $\eta_{\text{acc}} \sim 0.1$, the implied mass supplied to the engine is $M_{\text{sup}} \sim E_{\text{kin}}/(\eta_{\text{acc}} c^2) \sim 3 M_{\odot}$, corresponding to an effective accretion rate of $\dot{M} \sim 0.15 M_{\odot} \text{ s}^{-1}$ over the first ~ 20 s. These values lie well within the hyperaccretion regime expected during the prompt phase of Type I collapsars.

Furthermore, for mildly relativistic outflows relevant to low-luminosity GRBs, shell Lorentz factors in the range $\Gamma \sim 10\text{--}50$ can still produce internal-shock dissipation efficiencies of order $\epsilon_{\text{IS}} \sim 0.1$ (10%) when the shell-to-shell Lorentz-factor contrasts are moderate (Kobayashi et al. 1997; Daigne & Mochkovitch 2007). With an engine (accretion-to-jet) conversion efficiency $\eta_{\text{acc}} \sim 0.1$, this level of dissipation implies that the required mass-supply rate can be as low as $\dot{M} \sim 2 \times 10^{-3} M_{\odot} \text{ s}^{-1}$ to account for the prompt energetics, making the scenario naturally compatible with Type II collapsars sustained by longer-lasting, *fallback-motivated mass-supply histories* at relatively modest instantaneous rates.

Moreover, our simulation shows that the number of internal shock collisions exceeds the number of *observed* pulses. In practice, several closely spaced collisions may merge into a single pulse in the light curve, and the FWHM of individual pulses cannot be inferred directly from the collision list. Therefore, to measure pulse widths from the observed light curve itself, we first generated a smoothed version of the light curve using a Gaussian kernel ($\sigma = 2$ bins), which suppresses the high-frequency variability associated with individual collisions while preserving the broader pulse morphology. Local maxima in the smoothed light curve were then identified, and for each peak the left and right half-maximum crossing times were located by stepping outward from the peak and linearly interpolating between the grid points.

Furthermore, to observe the overall evolution of FWHMs with time, we applied a locally weighted regression (LOWESS; Cleveland 1979), which provides a non-parametric estimate of the FWHM– t_{pk} relation. As shown in Figure 1, the trend clearly shows mild fluctuations around a nearly constant value, consistent with the expectation in the mass-driven AMIS scenario. To assess the robustness of the result, further collisions with smaller peaks were added, and the FWHM trend remained the same.

4.2. Rate-Driven Scenario

In the rate-driven limit, the time-dependent mass-supply history to the central engine regulates the shell *ejection interval* within the AMIS framework:

$$\Delta t_i \propto \frac{1}{\dot{M}_{\text{ms}}(t_i)}, \quad L_i = c \Delta t_i, \quad (25)$$

while the shell masses remain nearly constant ($m_i \simeq m_0$). In the KPS model of internal shocks (Kobayashi et al. 1997), the separation of the shell L_i and the width of the shell ℓ_i are independent engine parameters. L_i represents the waiting time between consecutive ejections, and ℓ_i is set by the duration of the engine’s *ON* phase.

Therefore, unlike the original KPS treatment, we adopt a relation in which the duration of engine activity during each ejection episode is tied to the same mass-supply–controlled timescale within the AMIS framework,

$$\ell_i = c \delta t_{\text{ON}}(t_i), \quad \delta t_{\text{ON}}(t_i) \propto \Delta t_i, \quad (26)$$

so that periods of high mass-supply rate produce long engine-activity episodes and therefore thick shells, whereas a declining mass-supply history leads to progressively thinner shells.

With fixed shell masses, the dissipated energy in each collision is approximately constant, $E_{\text{int}} \propto m_0$, with random variations tied to the Lorentz-factor contrasts. Therefore, the resulting pulse properties are determined by the radial shock-crossing time, which scales with the shell thickness. When $\delta t_e \gg \tau_{\text{ang}}$, the peak luminosity follows the KPS scaling,

$$L_{\text{pk}}(t_i) \propto \frac{E_{\text{int}}}{\delta t_e(t_i)} \propto \frac{1}{\ell_i(t_i)}, \quad (27)$$

implying that thick shells produced during phases of enhanced mass-supply rate yield broad, low-luminosity pulses,

while the thinner shells ejected as the mass-supply history declines produce narrower and brighter pulses. When $\delta t_e \ll \tau_{\text{ang}}$, the angular timescale dominates and both the pulse width and L_{pk} saturate.

Our simulation of 70 shells with $m_i \simeq 3 \times 10^{28}$ g and $\Gamma_i \in [400, 800]$ yields a dissipated energy $E_{\text{diss}} \simeq 1.53 \times 10^{52}$ erg, out of an initial kinetic energy $E_{\text{kin}} \simeq 1.06 \times 10^{54}$ erg, corresponding to a time-averaged radiative efficiency $\epsilon \simeq 0.014$. The inverse relation between pulse width and peak luminosity emerges naturally, producing the width–luminosity evolution visible in Fig. 2. For a narrower Lorentz-factor distribution ($\Gamma \sim 10\text{--}50$), the effective mass-supply requirement reduces toward values compatible with longer-lasting, fallback-motivated feeding histories, as commonly discussed for Type II collapsar realizations.

To summarize, in this strict rate-driven formulation, the time-dependent mass-supply history modulates the ejection timing and shell thicknesses, and therefore regulates pulse widths. However, the pulse amplitudes do not directly follow the mass-supply envelope since E_{int} remains almost fixed. A more physical generalization, in which both Δt_i and the injected energy (or shell mass) scale with the instantaneous mass-supply rate, would imprint the same mass-supply–modulated profile on both the pulse widths and amplitudes, leading naturally to a smooth FRED-like envelope.

4.3. Global Envelope Characterization via Norris FRED Fitting

To quantify the large-scale temporal behavior of the mass-driven, mass-supply–modulated AMIS light curve, as an indicative example, we fit the simulated luminosity envelope using the analytic FRED form of Norris et al. (1996, 2005).

The pulse shape is (Norris et al. 2005; Hakkila & Preece 2014)

$$F(t) = A \exp \left[-\frac{\tau_1}{t - t_{\text{start}}} - \frac{t - t_{\text{start}}}{\tau_2} \right], \quad t > t_{\text{start}}, \quad (28)$$

where A is the pulse amplitude, t_{start} the effective onset time, and τ_1 and τ_2 the rise and decay timescales, respectively.

To perform a more reliable fit, we identified the significant envelope peaks in a Gaussian-smoothed version of the light curve and fitted only these points in logarithmic luminosity space. Figure 3 shows the fit together with the simulated AMIS envelope, with the posterior distributions of the MCMC fitting parameters ($\log A, t_{\text{start}}, \tau_1, \tau_2$) and their uncertainties. The best-fit parameters (defined as posterior median values with 68% credible intervals) are: $A = (2.83^{+2.18}_{-1.03}) \times 10^{51}$ erg s $^{-1}$, $t_{\text{start}} = 0.692^{+0.193}_{-0.303}$ s, $\tau_1 = 0.449^{+0.368}_{-0.258}$ s, and $\tau_2 = 13.242^{+3.147}_{-2.478}$ s, all of which fall within the observed distributions of bright long-GRB pulses (e.g., Norris et al. 1996; Kocevski et al. 2003; Bhat et al.

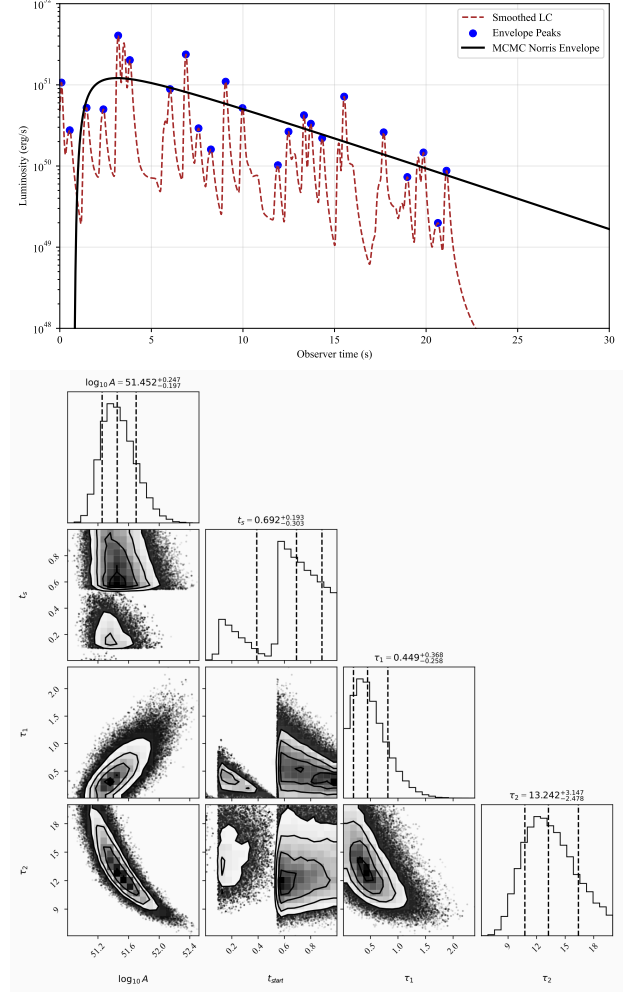


Figure 3. Norris et al. (2005) pulse fitting of the mass-driven AMIS luminosity envelope and the corresponding MCMC parameters. The blue points represent the most significant small pulse peaks used for the fit, the dashed curve shows the AMIS simulated luminosity, and the solid black line shows the Norris FRED profile. The full MCMC posterior distributions are shown in the corner plot, while the prior ranges and the posterior median values with 68% credible intervals are summarized in Table 1. Best-fit parameters (defined as the posterior median values with 68% credible intervals) are $A = (2.83^{+2.18}_{-1.03}) \times 10^{51}$ erg s $^{-1}$, $t_{\text{start}} = 0.692^{+0.193}_{-0.303}$ s, $\tau_1 = 0.449^{+0.368}_{-0.258}$ s, and $\tau_2 = 13.242^{+3.147}_{-2.478}$ s. The inferred FRED peak time, $t_{\text{pk}} = t_{\text{start}} + \sqrt{\tau_1 \tau_2} = 3.1 \pm 0.9$ s, coincides with the characteristic peak timescale of the imposed mass-supply envelope ($t_p = 3.5$ s).

2012; Hakkila & Preece 2014). We adopt uniform priors within the bounds listed in Table 1.

For the Norris et al. (2005) pulse model, the pulse-peak time is given analytically by $t_{\text{pk}} = t_{\text{start}} + \sqrt{\tau_1 \tau_2}$. Using the fitted values, we obtain $t_{\text{pk}} = 3.1 \pm 0.9$ s, in agreement with the characteristic timescale of the imposed mass-supply envelope in the simulation ($t_p = 3.5$ s).

Table 1. Priors and posterior constraints of the Norris FRED fit parameters derived from the MCMC analysis shown in Fig. 3. The priors correspond to the uniform bounds adopted in the MCMC sampling. Quoted uncertainties correspond to the 68% credible intervals.

Parameter	Prior range	Posterior median	68% interval
$A (\times 10^{51} \text{ erg s}^{-1})$	$[10^{-3}, 10^4]$	2.83	$^{+2.18}_{-1.03}$
$t_{\text{start}} (\text{s})$	$[0, 5.0]$	0.692	$^{+0.193}_{-0.303}$
$\tau_1 (\text{s})$	$[0.01, 20]$	0.449	$^{+0.368}_{-0.258}$
$\tau_2 (\text{s})$	$[0.1, 20]$	13.242	$^{+3.147}_{-2.478}$

4.4. A Note on Mass-Supply Mapping

In the current AMIS framework, we assume a *phenomenological* direct, power-law mapping between the time-dependent mass-supply history to the central engine, $\dot{M}_{\text{ms}}(t) \propto t^\beta$, and the modulated shell properties. Classical fallback accretion provides a physically motivated realization of such a mass-supply history, particularly relevant for Type II collapsars. This simplified assumption establishes the foundations of the framework and allows exploration of its fundamental observational signatures.

Variations in the mass-supply rate may introduce correlated changes in jet luminosity, mass-loading, and variability timescales. In fact, GRMHD simulations indicate that jet power depends non-linearly on the accretion rate—although the precise scaling exponent is uncertain—and is influenced by black hole spin, disk magnetic flux, and magnetization state (e.g., Tchekhovskoy et al. 2011; Liska et al. 2020; Gotlieb et al. 2022).

Future work that incorporates time-dependent GRMHD simulations of jet launching into the AMIS framework could replace the simple power-law mass-supply prescription with a physically consistent relation between accretion rate and shell properties, turning this first-order mapping into a more concrete, predictive quantity grounded in the engine physics.

We emphasize that the shell properties and pulse timescales derived within the AMIS framework correspond to intrinsic, source-frame dissipation timescales set by the engine-regulated mass-supply history. In realistic collapsar environments, these intrinsic pulse widths and luminosity trends may be further reshaped by jet collimation, propagation inside the stellar envelope, and viewing-angle effects, as demonstrated by multidimensional collapsar simulations (e.g., MacFadyen & Woosley 1999; MacFadyen et al. 2001). The AMIS framework is therefore intended to describe the engine-side boundary conditions for prompt emission, rather than to replace any sources of variability related to geometry. In this context, low-luminosity sources such as GRB 980425, which have often been discussed in terms of off-axis viewing, can also be naturally accommodated within the AMIS framework as intrinsically weak explosions characterized by modest

Lorentz factors and inefficient internal dissipation, without invoking an extreme viewing-angle geometry (e.g., Daigne & Mochkovitch 2007).

5. ENERGY-DEPENDENT PULSE WIDTHS IN MASS-SUPPLY-MODULATED GRBS

In the AMIS picture, as mentioned previously, the prompt emission is ultimately powered by accretion onto the central object, and the jet luminosity is assumed to scale with the instantaneous accretion rate. Once the mass-supply rate reaches its maximum at t_p and enters the decaying phase, the luminosity follows the expected power-law decline with an approximately constant decay index, which we adopt here as an indicative value, which for a fallback-modulated realization corresponds to $-5/3$.

Time-resolved spectral studies show that $E_p(t)$ evolves coherently with the instantaneous flux, either through hard-to-soft evolution or an intensity-tracking pattern (e.g., Lu et al. 2012; Yu et al. 2015). Therefore, motivated by observations, the evolution of the spectral peak energy is expected to follow the luminosity via

$$E_p(t) = E_0 \left[\frac{L_{\text{jet}}(t)}{L_0} \right]^{\gamma_{\text{ep}}}, \quad (29)$$

where E_0 and L_0 denote the peak energy and luminosity at t_0 , and γ_{ep} reflects the underlying emission physics.

Such correlations imply that the peak energy is closely related to the radiative process and the dissipation conditions in the emission region, potentially through variations in magnetic field strength, particle-acceleration efficiency, or other microphysical parameters (e.g., Moradi et al. 2024, and references therein).

The photon flux in a desired energy band $[E_1, E_2]$ is expressed as

$$N(t; E_1, E_2) = \frac{F_E(t) \varphi(E_p(t))}{E_p(t) \varphi_0},$$

$$\varphi(E_p) = \int_{E_1/E_p}^{E_2/E_p} B(x) dx, \quad (30)$$

where $F_E(t)$ is the bolometric energy flux, $\varphi_0 = \int_0^\infty x B(x) dx$ is a normalization constant, and $B(x)$ is the standard normalized Band function (Band et al. 1993). If the Band indices α and β are treated as constants, then $\varphi(E_p(t))$ acts merely as a multiplicative factor for each band, and all different energy bands exhibit identical temporal pulse widths.

Observations and modeling show that the Band indices are effectively energy-dependent: the low-energy slope α correlates with the energy dependence of GRB pulse widths (Peng et al. 2012), and analyses of individual GBM bursts demonstrate that the fitted α changes when the low-energy band-

pass is varied (Tierney et al. 2013). Simulations further confirm that, even for a fixed intrinsic spectrum, the recovered α depends on the instrumental bandpass because different portions of the curved spectrum are sampled (Burgess et al. 2015).

To account for this, we adopt a simple phenomenological model in which the low-energy index depends on photon energy,

$$\alpha(E) = \alpha_0 + k \log \frac{E}{E_{\text{ref}}}, \quad (31)$$

where α_0 is the index at a reference energy E_{ref} , and k is a positive constant, consistent with observations. Substituting this into the asymptotic low-energy regime ($E < E_p$), the photon flux in a given band reads

$$\begin{aligned} N_{\text{low}}(t; E) &\propto L_{\text{jet}}(t) [E_p(t)]^{-(2+\alpha(E))} \\ &\propto \left(\frac{t}{t_0}\right)^{-\frac{5}{3}[1-\gamma_{\text{ep}}(2+\alpha(E))]} . \end{aligned} \quad (32)$$

Because $\alpha(E)$ increases at lower energies, the effective decay index is smaller for low-energy bands, producing broader pulses, whereas higher-energy bands with smaller $\alpha(E)$ decay faster and result in narrower pulses. A similar argument applies to the high-energy tail through $\beta(E)$.

This energy-dependent behavior can reproduce the observed scaling of pulse width with energy, $w(E) \propto E^{-0.4}$ (e.g., Norris et al. 1996; Yu et al. 2015). The coupling parameter γ_{ep} controls how the evolution of the peak energy modulates the decay, but reproducing the observed scaling requires adjusting the phenomenological parameters α_0 , k , and γ_{ep} . Future iterations of the AMIS model should therefore explicitly include energy- and possibly time-dependence of the Band indices to self-consistently model the temporal evolution and pulse-width scaling of GRB emission.

6. DISCUSSIONS AND CONCLUSIONS

This work presents a framework in which the time dependence of the engine mass-supply history, arising from collapse-driven mass delivery and delayed feeding of bound material, shapes the prompt emission of long GRBs. In this picture, the broad temporal envelope of the burst reflects the smooth rise and decay of the effective mass-supply rate to the central engine, while the rapid variability is produced by stochastic fluctuations in the Lorentz factors and the masses or ejection intervals of individual shells that collide through internal shocks. Within the standard collapsar scenario, Type I collapsars, with rapid black-hole formation and high early accretion rates, and Type II collapsars—with longer-lasting, fallback-like feeding histories, can both produce such behavior. The AMIS calculations shown here demonstrate that a FRED-like envelope naturally emerges whenever the mass-supply history undergoes a smooth rise followed by a power-law decay, in physically motivated real-

izations where such a decay is present, while the fine temporal structure arises from shell-to-shell fluctuations that generate the multi-peaked profiles commonly observed in GRB prompt emission.

Two cases were explored: 1) In the *mass-driven* scenario, the time-dependent mass-supply rate primarily modulates the masses of the ejected shells while the ejection rate remains nearly constant. Individual pulses tend to maintain comparable widths while their amplitudes follow the envelope imposed by the mass-supply history. 2) In the *rate-driven* scenario, in turn, the shell masses remain roughly constant and the time-dependent mass-supply rate modulates the shell widths and consequently the ejection intervals. In this case, pulses broaden and dim during phases of high mass-supply rate and narrow as the mass-supply rate declines.

Two restrictions of the present implementation should be noted. *First*, the mapping between the time-dependent mass-supply history and the engine outflow in both explored cases is still phenomenological. A more physically grounded connection requires GRMHD simulations of a time-dependent accretion disk and jetted outflow. *Second*, the temporal evolution of the spectral peak energy $E_p(t)$ is imposed externally, albeit with physical motivation. Extensive time-resolved spectral analyses show that $E_p(t)$ tracks the instantaneous flux, either through a hard-to-soft decay or an intensity-tracking relation (e.g., Lu et al. 2012; Yu et al. 2015).

This behavior suggests that the peak energy is closely associated with the dissipation physics and the engine power. A more complete formulation of AMIS should therefore derive the evolution of E_p self-consistently from the engine power, parameterized by the accretion rate, and the outflow Lorentz factor, rather than imposing it externally.

Regarding efficiency, for typical Lorentz-factor fluctuations in the range $\Gamma \sim 10\text{--}1000$, the global radiative efficiency is $\epsilon_{\text{rad}} \sim 0.01\text{--}0.2$, consistent with classical internal-shock expectations, where the dissipated fraction is limited by the Lorentz-factor contrasts and the distribution of shell masses.

In addition, alternative hybrid scenarios are worth considering. If the outflow is magnetically dominated, dissipation may proceed through reconnection rather than shocks. In magnetic reconnection scenarios such as the ICMART model (Zhang & Yan 2011), the time-dependent mass-supply history still dictates the overall luminosity, but energy release occurs through reconnection-driven episodes that are intrinsically more efficient than internal shocks. Such a picture retains the smooth envelope and rapid variability characteristic of AMIS while offering a path toward higher radiative efficiency.

Future work should aim at connecting time-dependent mass-supply physics and jet properties using GRMHD

simulations, and at testing the model quantitatively with large samples of GRBs. Combining the AMIS framework with time-resolved fitting of pulse properties, widths, and spectral evolution may help determine whether mass-supply–modulated (fallback-motivated where applicable) variability is a viable explanation for the prompt phase and what it reveals about the structure of the progenitor and the central engine. We emphasize that AMIS describes an intrinsic, engine-level modulation that provides the primary organizing timescale and luminosity structure of the prompt emission; jet propagation and viewing-angle effects may in-

duce secondary distortions and event-to-event scatter, but do not generically erase the mass-supply–imprinted temporal trends predicted by the model.

We are grateful to the referee for their valuable and constructive feedback, which helped improve the manuscript. R.M thanks S. Kobayashi for useful discussions and suggestions. The authors used an AI-based tool solely for language polishing. R. Moradi acknowledges support from the Academy of Sciences Beijing Natural Science Foundation (IS24021) and the Institute of High Energy Physics, Chinese(E32984U810).

REFERENCES

An, Z. H., Sun, X. L., Zhang, D. L., et al. 2022, *Radiation Detection Technology and Methods*, 6, 43.
<https://doi.org/10.1007/s41605-021-00289-y>

Aptekar, R. L., Frederiks, D. D., Golenetskii, S. V., et al. 1995, *SSRv*, 71, 265

Band, D., Matteson, J., Ford, L., et al. 1993, *ApJ*, 413, 281

Bhat, P. N., Briggs, M. S., Connaughton, V., et al. 2012, *ApJ*, 744, 141

Bošnjak, Ž., Daigne, F., & Dubus, G. 2009, *A&A*, 498, 677

Bošnjak, Ž., Barniol Duran, R., & Pe’er, A. 2022, *Galaxies*, 10, 38

Bošnjak, Ž., & Daigne, F. 2014, *A&A*, 568, A45

Burgess, J. M., Ryde, F., & Yu, H.-F. 2015, *MNRAS*, 451, 1511

Chevalier, R. A. 1989, *ApJ*, 346, 847

Cleveland, W. S. 1979, *Journal of the American Statistical Association*, 74, 829

Daigne, F., & Mochkovitch, R. 1998, *MNRAS*, 296, 275
—. 2003, *MNRAS*, 342, 587
—. 2007, *A&A*, 465, 1

Fishman, G. J., Meegan, C. A., Parnell, T. A., et al. 1985, in *International Cosmic Ray Conference*, Vol. 3, 19th International Cosmic Ray Conference (ICRC19), Volume 3, ed. F. C. Jones, 343–346

Fryer, C. L., Woosley, S. E., & Hartmann, D. H. 1999, *The Astrophysical Journal*, 526, 152

Geng, J. J., Wu, X. F., Huang, Y. F., & Yu, Y. B. 2013, *ApJ*, 779, 28

Gottlieb, O. 2025, *ApJL*, 992, L3

Gottlieb, O., Lalakos, A., Bromberg, O., Liska, M., & Tchekhovskoy, A. 2022, *MNRAS*, 510, 4962

Guidorzi, C., Dichiara, S., Frontera, F., et al. 2015, *The Astrophysical Journal*, 801, 57

Hakkila, J., & Preece, R. D. 2014, *ApJ*, 783, 88

Hascoët, R., Daigne, F., & Mochkovitch, R. 2012, *A&A*, 542, L29

Hintze, H. 2022, Master’s thesis, KTH Royal Institute of Technology, analyzed 2710 *Fermi* GRBs and found ~48% of long bursts to be single-peaked.
<https://urn.kb.se/resolve?urn=urn:nbn:se:kth:diva-313589>

Jacquemin-Ide, J., Gottlieb, O., Lowell, B., & Tchekhovskoy, A. 2024, *ApJ*, 961, 212

Kobayashi, S., Piran, T., & Sari, R. 1997, *ApJ*, 490, 92

Kocevski, D., Ryde, F., & Liang, E. 2003, *ApJ*, 596, 389

Komissarov, S. S., & Barkov, M. V. 2009, *MNRAS*, 397, 1153

Kumar, P., Narayan, R., & Johnson, J. L. 2008, *MNRAS*, 388, 1729

Kumar, P., & Zhang, B. 2015, *PhR*, 561, 1

Li, X. Q., Wen, X. Y., An, Z. H., et al. 2022, *Radiation Detection Technology and Methods*, doi:10.1007/s41605-021-00288-z

Liska, M., Tchekhovskoy, A., & Quataert, E. 2020, *MNRAS*, 494, 3656

Lu, R.-J., Wei, J.-J., Liang, E.-W., et al. 2012, *ApJ*, 756, 112

Maccary, R., Guidorzi, C., Maistrello, M., et al. 2026, *Journal of High Energy Astrophysics*, 49, 100456

MacFadyen, A. I., & Woosley, S. E. 1999, *ApJ*, 524, 262

MacFadyen, A. I., Woosley, S. E., & Heger, A. 2001, *ApJ*, 550, 410

Maxham, A., & Zhang, B. 2009, *ApJ*, 707, 1623

Meegan, C., Lichti, G., Bhat, P. N., et al. 2009, *ApJ*, 702, 791

Mészáros, P. 2006, *Reports on Progress in Physics*, 69, 2259.
<http://stacks.iop.org/0034-4885/69/i=8/a=R01>

Moradi, R., Wang, C. W., Zhang, B., et al. 2024, *ApJ*, 977, 155

Nakar, E., & Piran, T. 2002, *ApJL*, 572, L139

Narayan, R., Piran, T., & Kumar, P. 2001, *ApJ*, 557, 949

Norris, J. P., Bonnell, J. T., Kazanas, D., et al. 2005, *ApJ*, 627, 324

Norris, J. P., Nemiroff, R. J., Bonnell, J. T., et al. 1996, *ApJ*, 459, 393

Peng, Z. Y., Zhao, X. H., Yin, Y., Bao, Y. Y., & Ma, L. 2012, *ApJ*, 752, 132

Popham, R., Woosley, S. E., & Fryer, C. 1999, *ApJ*, 518, 356

Ramirez-Ruiz, E., & Fenimore, E. E. 2000, *ApJ*, 539, 712

Rees, M. J., & Meszaros, P. 1994, *ApJL*, 430, L93

Ryde, F., & Svensson, R. 2000, *ApJL*, 529, L13

—. 2002, *ApJ*, 566, 210

Sari, R., & Piran, T. 1996, in American Institute of Physics Conference Series, Vol. 384, Gamma-ray Bursts: 3rd Huntsville Symposium, ed. C. Kouveliotou, M. F. Briggs, & G. J. Fishman, 782–786

Sari, R., & Piran, T. 1997, *MNRAS*, 287, 110

Tchekhovskoy, A., Narayan, R., & McKinney, J. C. 2011, *MNRAS*, 418, L79

Tierney, D., McBreen, S., Preece, R. D., et al. 2013, *A&A*, 550, A102

Wang, C. W., Zhang, J., Zheng, S. J., et al. 2024, *Experimental Astronomy*, 57, 26

Wang, X.-Y., & Mészáros, P. 2007, *ApJ*, 670, 1247

Wu, X.-F., Hou, S.-J., & Lei, W.-H. 2013, *ApJL*, 767, L36

Yu, H.-F., van Eerten, H. J., Greiner, J., et al. 2015, *A&A*, 583, A129

Zhang, B. 2018, *The physics of gamma-ray bursts* (Cambridge University Press)

Zhang, B., & Yan, H. 2011, *ApJ*, 726, 90

Zhang, D. L., Zheng, C., Liu, J. C., et al. 2023, *Nuclear Instruments and Methods in Physics Research A*, 1056, 168586

Zhang, J.-P., Wang, C.-W., Yu, Z.-H., et al. 2025, arXiv e-prints, arXiv:2509.26283

Zhang, S., Zhang, S. N., Lu, F. J., et al. 2018, in Society of Photo-Optical Instrumentation Engineers (SPIE) Conference Series, Vol. 10699, *Space Telescopes and Instrumentation 2018: Ultraviolet to Gamma Ray*, ed. J.-W. A. den Herder, S. Nikzad, & K. Nakazawa, 106991U

Zhang, S.-N., Li, T., Lu, F., et al. 2020, *Science China Physics, Mechanics, and Astronomy*, 63, 249502

Zhang, W., Woosley, S. E., & Heger, A. 2008, *ApJ*, 679, 639